ELSEVIER

Atmospheric Research 39 (1995) 287–311

ATMOSPHERIC RESEARCH

A squall-like narrow cold-frontal rainband diagnosed by combined thermodynamic and cloud microphysical retrieval

Bart Geerts [a,*], Peter V. Hobbs [b]

[a] *Earth System Science Lab, University of Alabama in Huntsville, Huntsville, USA*
[b] *Atmospheric Sciences Department, University of Washington, Seattle, USA*

Received 3 November 1994; accepted 11 April 1995

Abstract

Doppler radar, airborne, and sounding data are used to describe the structure of an exceptionally vigorous narrow cold-frontal rainband (NCFR). A combined thermodynamic and cloud microphysical retrieval technique is used to derive the pressure perturbations and buoyancy in balance with the flow field in the vicinity of the NCFR.

The NCFR was triggered by a well-defined cold front that penetrated beneath a deep layer of conditionally unstable prefrontal air. The rainband, which persisted for ~6 h, was located over the Gulf Stream, just off the mid-Atlantic Coast of the U.S.A. It consisted of a series of short-lived cells with updraft maxima between 5 and 15 m s^{-1} and tops around 12 km. The updraft associated with the NCFR was driven primarily by buoyancy in the middle troposphere, which explains its convective nature. Trailing behind the NCFR was a broad region of stratiform precipitation.

Pressure perturbations in the NCFR and the trailing stratiform region were produced mainly by a combination of frontal convergence and buoyancy opposition. The pressure perturbations surrounding the cells within the rainband were due primarily to strong updrafts in the presence of wind shear parallel to the rainband.

The same dynamic and cloud microphysical processes that operate in stratiform regions behind some squall lines were present in this NCFR. However, in contrast to a squall line with a trailing stratiform region, the low-level cold pool that penetrated beneath the NCFR was maintained primarily by strong cold advection, rather than by evaporational cooling in a shallow rear-to-front flow. The preponderance of advective over diabatic cooling can be used as a criterion to diagnostically differentiate between NCFRs and squall lines.

* Corresponding author.

SSDI 0169-8095(95)00018-6

1. Introduction

Narrow cold-frontal rainbands (NCFRs) are typically shallow and the environment in which they form is generally convectively neutral, or only locally slightly unstable (e.g., Browning and Harrold, 1970; Hobbs and Biswas, 1979; Carbone, 1982; Hobbs and Persson, 1982; Bond and Fleagle, 1985). Detailed studies by Parsons et al. (1987) and Roux et al. (1993) show that the updrafts in NCFRs are driven by frontal convergence; the low-level circulation acts essentially as a density current, since the leading edge of the front is coincident with a high-pressure anomaly and the updraft at the leading edge is maintained by a dynamically induced vertical pressure perturbation gradient, rather than by buoyancy. Parsons (1992) demonstrates that in a environment nearly neutral to moist ascent a strong updraft (and associated NCFR) can be maintained at the leading edge of a density current, if the prefrontal low-level shear over the depth of the cold pool is in the same direction as, and of similar strength to, the density current.

Squall lines are often followed by regions of stratiform precipitation (e.g., Smull and Houze, 1985; Chong et al., 1987; Houze et al., 1989; Biggerstaff and Houze, 1991). The organization of both the convection and the stratiform rain is explained by buoyancy forcing, which is primarily due to latent heating and cooling (e.g., Rutledge and Houze, 1987; Fovell and Ogura, 1988; Roux, 1988). The relationship between a squall line and its trailing stratiform region is symbiotic (Houze, 1993); the essential environmental conditions are a deep conditionally unstable layer ahead of the squall line and a dry middle-level, rear-to-front flow. Synoptic-scale variability (such as a surface or upper-level trough) does not appear to be a necessary component in the organization of squall lines.

Convective systems are often triggered and organized by a synoptic-scale discontinuity, such as a cold front. However, it is not clear how, in such a situation, frontal and convective dynamics interact. To examine these interactions, we present in this paper a case study of a frontal rainband that in all respects resembled a squall line with a trailing stratiform region. This rainband occurred in winter off Cape Hatteras, North Carolina, near the axis of the Gulf Stream. The rainband, which was located just ahead of a well-defined, deep cold front, was detectable on radar for ~ 6 h. It consisted of a series of transient cells with tops around 12 km. Based on the classification of Hobbs (1978), this rainband is referred to as a NCFR; however, it was quite different from any NCFR previously described. While the NCFR was located near the axis of the Gulf Stream, the interplay between convective and frontal dynamics of the kind observed here is undoubtedly not confined to this location.

The evolution of the NCFR is examined with the aid of sub-synoptic scale surface analyses, and data from an incoherent radar (WSR-57), Doppler radars (NCARs CP-3 and CP-4), a research aircraft, and dropsondes, which were available as part of the Genesis of Atlantic Lows Experiment (GALE) (Dirks et al., 1988).

The kinematic structure of the NCFR is derived using the ground-based 5 cm dual-Doppler radar data. The airflow field is related to the dynamics of the rainband by means of a technique of combined *t*hermodynamic and cloud *m*icrophysical *r*etrieval (TMR), which relates thermodynamic and cloud microphysical variables to an input flow field, and to each other, in a self-consistent way, using all of the equations of motion, the water continuity equations, and specified boundary values. This technique can provide insights into the pressure perturbation and buoyancy fields that force an observed flow field and

precipitation structure. The TMR technique used here has been described by Geerts and Hobbs (1991). In essence, the buoyancy field is estimated from a combination of momentum constraints and the first law of thermodynamics. The latent heating, which is needed in the first law, is estimated from a bulk parameterized water continuity model, using water vapor, cloud water, cloud ice, rain and snow. Pressure perturbations are then calculated using momentum constraints. The basic assumptions in this application of the TMR technique are that the flow is steady and two-dimensional.

Previously two studies have analyzed the dynamical structure of a NCFR by means of a retrieval technique (Parsons et al., 1987; Roux et al., 1993). Our TMR technique differs from that employed by Roux et al. (1993) in that the prognostic bulk water continuity equations are an integral part of the retrieval scheme, which obviates the need to parameterize latent heating in terms of observed radar reflectivity and sounding data. Parsons et al. (1987) retrieved 3-D pressure perturbations and buoyancy from the momentum equations only.

In the following section we describe the mesoscale structure of the NCFR. The airflow and reflectivity derived from dual-Doppler radar data are discussed in Section 3. In Section 4 we analyze the cloud microphysical and dynamical structure of the NCFR. Conclusions are presented in Section 5.

2. Mesoscale structure of the NCFR

Starting at ~ 1800 UTC 26 January 1986, deep convection developed off Cape Hatteras ahead of a deep cold front. The cold front was originally mainly a middle-tropospheric feature, but as it moved across the East Coast of the U.S.A. south of Cape Hatteras it developed at the surface (Martin et al., 1990). This occurred as the deep cold front merged with the remnants of a shallow coastal front (described by Riordan, 1990), that had moved offshore during the 15 h prior to 2100 UTC. During the same period, a broad low-pressure system located over southern Georgia at 0900 UTC (Fig. 1) deepened and moved northeastward. By 2100 UTC the cold front had moved entirely offshore along the mid-Atlantic Coast of the U.S.A. From 2100 to 0300 UTC the next day, the broad low deepened rapidly along the North-Atlantic Coast of the U.S.A. (Locatelli et al., 1994). The synoptic evolution of the deep cold front has been described by Martin et al. (1993).

From 1800 UTC 26 January to 0500 UTC 27 January, five rainbands were observed during the passage of the frontal system. The first two were warm-sector rainbands with a cellular structure, these rainbands developed offshore and remained intact for at least as long as they were within range of the Cape Hatteras WSR-57 radar. The last two rainbands, which were wide cold-frontal, were more stratiform in nature and associated with low-level convergence and an increased slope of the frontal surface aloft (Locatelli et al., 1994).

In this paper we focus on the third rainband, which was the NCFR. This rainband first appeared at 1930 UTC as a line of precipitation to the southwest of Cape Hatteras, and it developed vigorously offshore after 2100 UTC. During its entire lifetime, until 0130 UTC 27 January, the NCFR consisted of a series of relatively short-lived convective cells about 10 km in diameter. Two closely spaced cells developed around 2155 UTC. At 2220 UTC, when these cells reached their maximum intensity, they were located near the right hand edge of Fig. 2. These cells will be examined in detail in this paper. Around 2235 UTC these

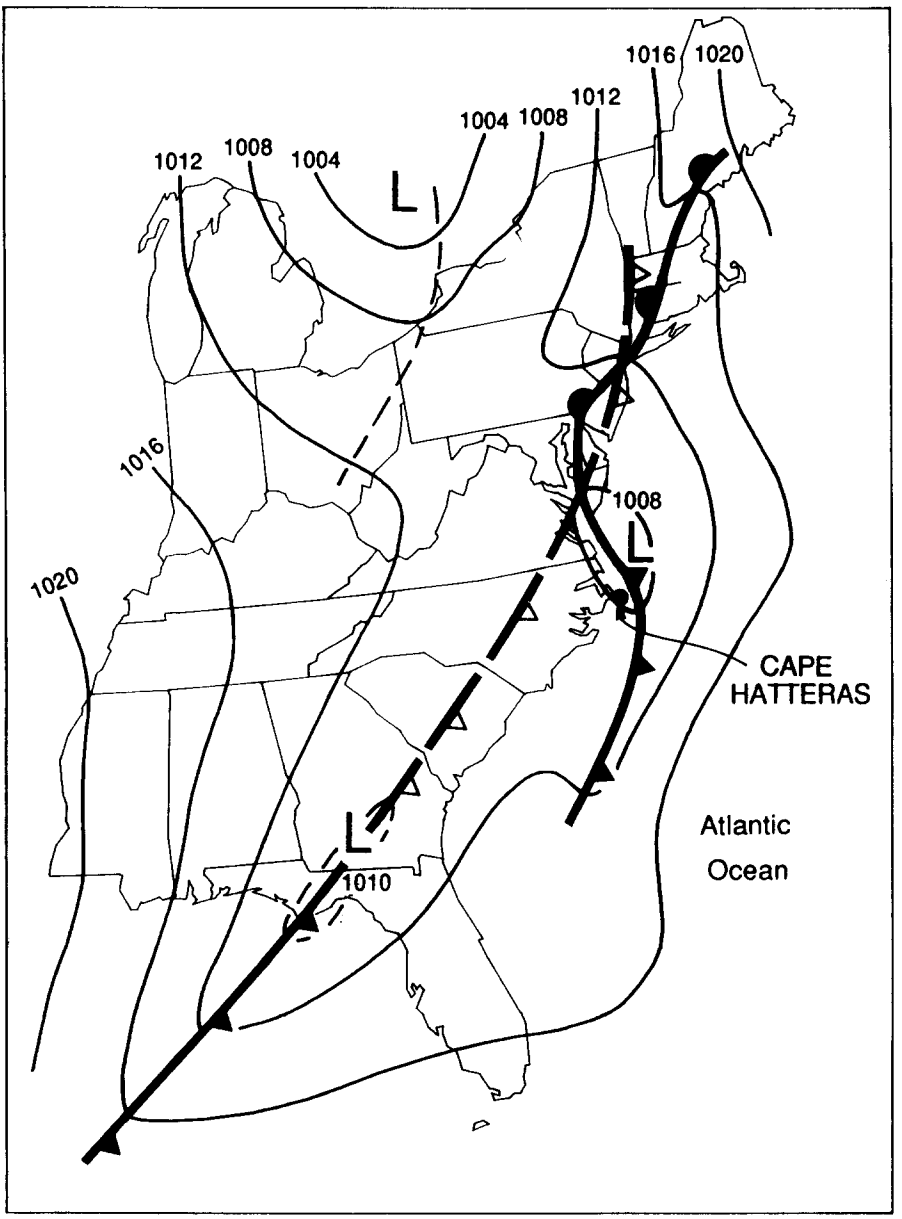

Fig. 1. Sea-level pressure (in hPa) at 0900 UTC on 26 January 1986. The deep tropospheric cold front aloft is indicated by unfilled cold frontal symbols along a dashed line. Surface cold and warm fronts are shown by conventional filled symbols along solid lines.

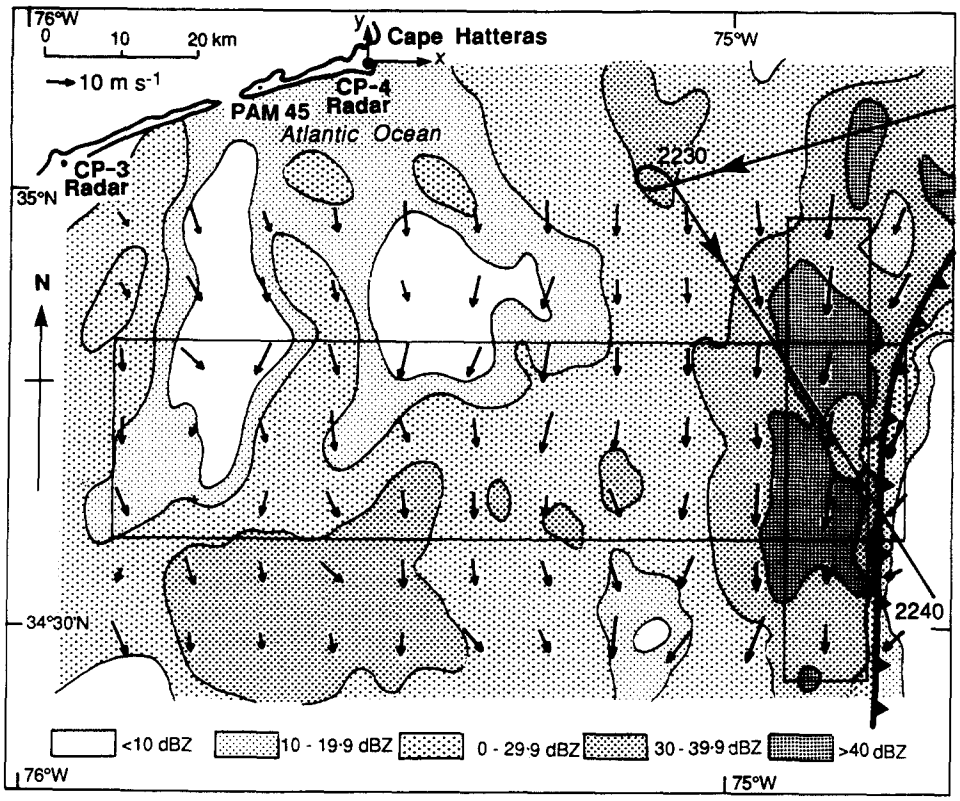

Fig. 2. Radar reflectivity of the NCFR and the trailing stratiform region at an altitude of 1.5 km measured by the CP-4 radar at 2220 UTC on 26 January 1986. Increasing intensities of shading correspond to increasing values of the reflectivity as indicated by the key. The thicker line in the NW corner of the map is the North Carolina coastline. The locations of the CP-3 and CP-4 Doppler radars and the PAM-II surface mesonet station #45 are indicated. Superimposed on the radar reflectivity are vectors of storm-relative wind at 1.5 km, derived from the CP-3 and CP-4 Doppler radars. The flight track of the NOAA P-3 aircraft, flying at an altitude of 280 m, is shown by the arrowed line (with time in UTC) in a storm-relative frame centered at 2220 UTC. The approximate position of the surface cold front at 2220 UTC is indicated by standard symbols. Two rectangular boxes are shown: in the E–W elongated box 3-D air velocities derived from the Doppler radars were contracted into a cross section across the NCFR (the *across-section*); in the N–S elongated box in the SE corner of the map 3-D air velocities were contracted into a cross section along the NCFR (the *along-section*).

cells, which were still well within radar echo range, dissipated and new cells developed along the line of the NCFR.

In Fig. 2, the radar echoes to the east of the NCFR display little organization. The NOAA WP-3D aircraft observed a windshift from about 350° behind the front to 60° ahead of the front at an altitude of 280 m. There was no evidence of a low-level prefrontal jet. When the aircraft crossed the front at 2237 UTC (Fig. 2), it encountered intense turbulence and a temperature rise of ~ 2°C. The across-front convergence, estimated from the 2230–2240 UTC flight track, reached a peak value of $\sim 2 \times 10^{-3}\ s^{-1}$.

Temperature profiles ahead and well to the rear of the NCFR are shown in Fig. 3a. The sounding ahead of the NCFR is based on a dropsonde released just ahead of the front from

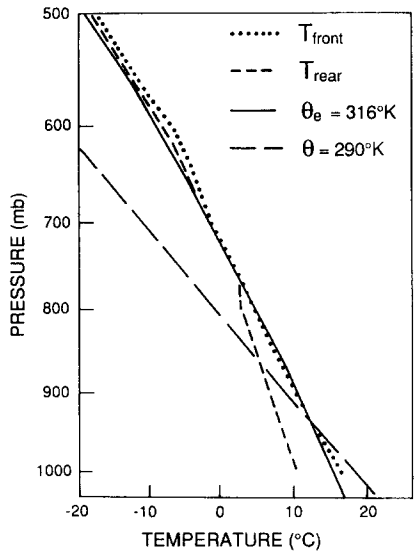
500
600
700
800
900
1000
PRESSURE (mb)
-20
-10
0
10
20
TEMPERATURE (°C)
T_{front}
T_{rear}
θ_e = 316°K
θ = 290°K

(a)

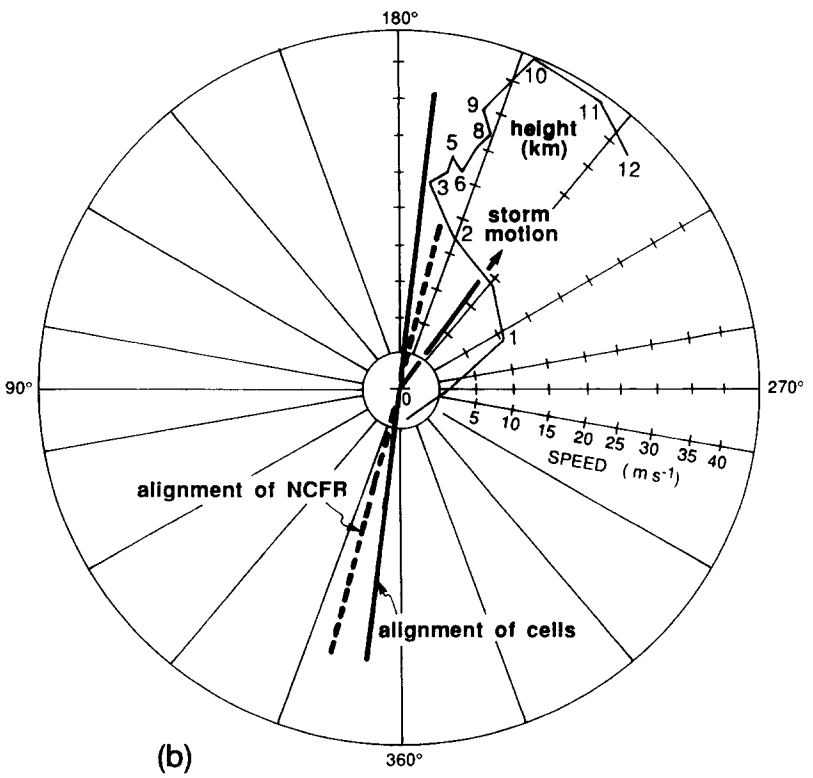
180°
90°
270°
360°
height (km)
storm motion
alignment of NCFR
alignment of cells
SPEED (m s-1)
5 10 15 20 25 30 35 40

(b)

the NOAA P-3 aircraft at 5.7 km altitude. To obtain an entire profile ahead of the front, the temperature and humidity data at the nearest gridpoint in the 0000 UTC 27 January initialization of the National Weather Service's Nested Grid Model (NGM) were used above 5.7 km. The total integrated water in the composited sounding was 34.4 mm, which corresponds to an average relative humidity of 87%. The oceanic boundary layer is almost saturated, but from 2 to 4 km the air is slightly drier.

The sounding behind the front is based on the 2220 UTC Cape Hatteras radiosonde. This sounding is close to saturation below 500 hPa, except for a drier layer centered at 780 hPa (where the relative humidity was 61%). The cooling of 2–5°C across the NCFR below 800 hPa is indicative of a cold-frontal passage. There is slight warming in the middle troposphere. The profile ahead of the front is almost entirely potentially unstable below 600 hPa. This suggests that convective dynamics were important. The level of neutral buoyancy in this profile is at 9.5 km. However, radar data and satellite imagery show that the tops of the cells were between 12 and 13 km. The convective available potential energy (CAPE) in this profile is ~ 820 J kg^{-1}. The air ahead of the front may have contained more CAPE. The dropsonde used to represent prefrontal conditions was released close to the rainband in an area of scattered, shallow convection. This may also explain the virtual absence of negative energy along the ascent path of an air parcel from the surface, and the deep layer of nearly saturated air.

The NCFR was oriented about 15° clockwise of north–south (Fig. 3b), whereas, the two cells were aligned north–south. The counterclockwise alignment of the cells relative to the NCFR contrasts with the clockwise orientation of cores relative to NCFRs studied off the Pacific Coast of the U.S.A. (Hobbs and Biswas, 1979; Hobbs and Persson, 1982). Other cells in the NCFR were aligned roughly parallel to the NCFR. The two cells in Fig. 2 move to the northeast, in a direction about 30° clockwise of their orientation. We will refer to this cell motion as the *storm motion* (Fig. 3b).

The wind profile from the Hatteras sounding (Fig. 3b) is representative of the region behind the NCFR. This profile shows a strong backing of the wind from the surface (where there was a weak wind from the north) to 3 km (where the wind was 28 m s^{-1} from the south), indicating cold-air advection. This implies that a cold front passed Cape Hatteras, and that the frontal surface was at an altitude between ~ 2.5 and 3 km. The vertical shear in the frontal zone between ~ 1 and 3 km was from the southeast, which was about 40° counterclockwise of the orientation of the NCFR (Fig. 3b). Since the 1000–700 hPa thermal wind was oriented approximately parallel to the NCFR, the ageostrophic flow at the base of the frontal zone must have had a westerly component relative to the ageostrophic wind at the top of the frontal zone. This is characteristic of a frontal secondary circulation.

The wind profile above the frontal zone had a large amount of helicity (defined as the vertically integrated inner product of vertical vorticity and storm-relative velocity). Con-

Fig. 3. a. Temperature profile ahead of (T_{front}) and behind (T_{rear}) the cold front. T_{front} is based on a dropsonde from the NOAA P-3 at 2128 UTC. T_{rear} is based on the Cape Hatteras sounding released at 2220 UTC. The moist adiabat for an equivalent potential temperature (θ_e) of 316 K, and the dry adiabat for a potential temperature (θ) of 290 K, are shown. The profile of T_{front} (T_{rear}) is used as the eastern (western) boundary condition in the across-section.

b. Hodograph based on the Cape Hatteras sounding released at 2220 UTC. Also shown are the storm motion (i.e., the displacement speed of the two cells in Fig. 2), the alignment of the two cells, and the orientation of the NCFR.

vective storms in an environment with high helicity experience less turbulent dissipation and may therefore be more stable (Lilly, 1986). The storm-relative velocity profile, derived from Doppler radar data within the NCFR (in the north–south elongated rectangular box in Fig. 2), shows veering of the storm-relative flow throughout the volume above 1 km, similar to the upstream profile in Fig. 3b. The vertical vorticity profile within the same box is cyclonic at all levels, and the vorticity is strongest between 5 and 6 km altitude. Helicity production is only possible if cyclonic vorticity and buoyancy within the storm are positively correlated (Lilly, 1986). The presence of helicity in the environment (Fig. 3b) and within the storm (not shown) suggests (although it does not prove) that the storm circulation was driven by buoyancy. In short, the soundings indicate a combination of frontal and convective dynamics.

We will analyze both an east–west section across the NCFR and its trailing region (the *across-section*), and a north–south section along the two cells (the *along-section*). The reflectivity and velocity data for these sections are those contained within the two boxes shown in Fig. 2. The long axes of these boxes are the horizontal axes in the cross-sections; the short axes of the boxes indicate the width over which the radar reflectivity and Doppler velocity data were averaged. For example, the across-section is an average of all x–z sections between 40 and 60 km south of CP-4. The across-section better represents the frontal system. However, we will also show the along-section because the storm-relative flow and shear were mostly meridional at low levels (Fig. 2). Consequently, the along-section is a better 2-D approximation to the 3-D airflow pattern; it also reveals the cellular nature of the NCFR.

3. Airflow and radar reflectivity

The horizontal airflow fields through the NCFR and its trailing stratiform region were derived from dual-Doppler radar data. The vertical velocity was derived from the horizontal airflow field using the anelastic continuity equation in 3-D. Since the rainband was quite deep, uncertainties in the surface convergence produce errors in the derived vertical velocity that quadruple from the surface to cloud top due to the decrease in air density. These uncertainties were potentially large because the NCFR was located near the outer range of the dual-Doppler radar lobe. To avoid this problem, the continuity equation was integrated downward. A rectangular domain is needed for TMR. The domain of Doppler radar data was irregular both at upper levels (no data above the trailing region) and near the surface (no data below 1 km near the NCFR). Therefore, to make TMR possible, and to retain at least the bulk of the vertical structure of the NCFR and its trailing region, a few missing velocity data points were added, by interpolating between the Doppler radar data and the sounding data. The vertical velocity was regressed to zero at sea level.

Because the TMR is 2-D, the airflow must be balanced in 2-D. Following the technique of Hauser and Amayenc (1986), a 2-D mass balance was imposed by defining a stream-function that best represented (in a least-squares sense) the radar-derived 2-D flow in the cross section. The 2-D mass-balanced, storm-relative airflow field through the across-section is shown in Fig. 4, where it is superimposed on the radar reflectivity.

In structure, size, and depth, this section is strikingly similar to a cross section through a squall line with a trailing stratiform region (e.g., Biggerstaff and Houze, 1991, Biggerstaff

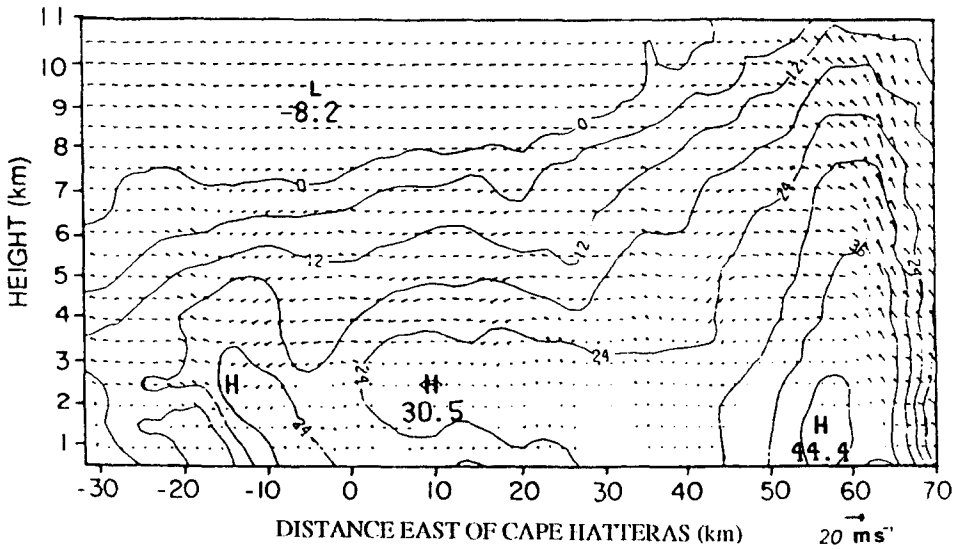

Fig. 4. Airflow field in the across-section derived from Doppler radar data. The radar reflectivity is contoured in 6 dBZ increments.

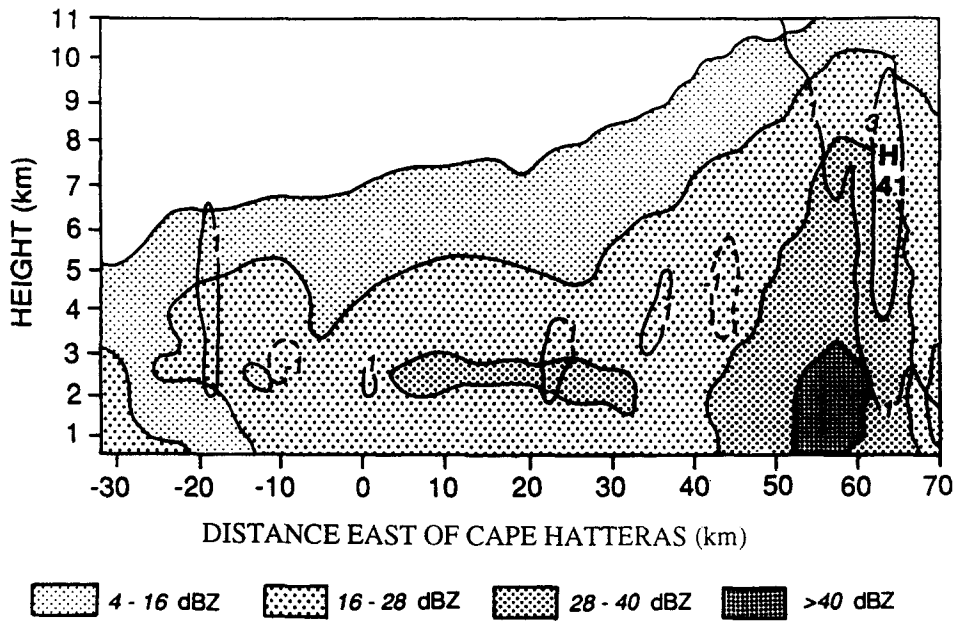

Fig. 5. Vertical air velocities (in m s^{-1}) in the across-section. Positive contours (upward motions) are solid, negative contours (downward motions) are dashed. The radar reflectivity is shaded according to the key in the figure.

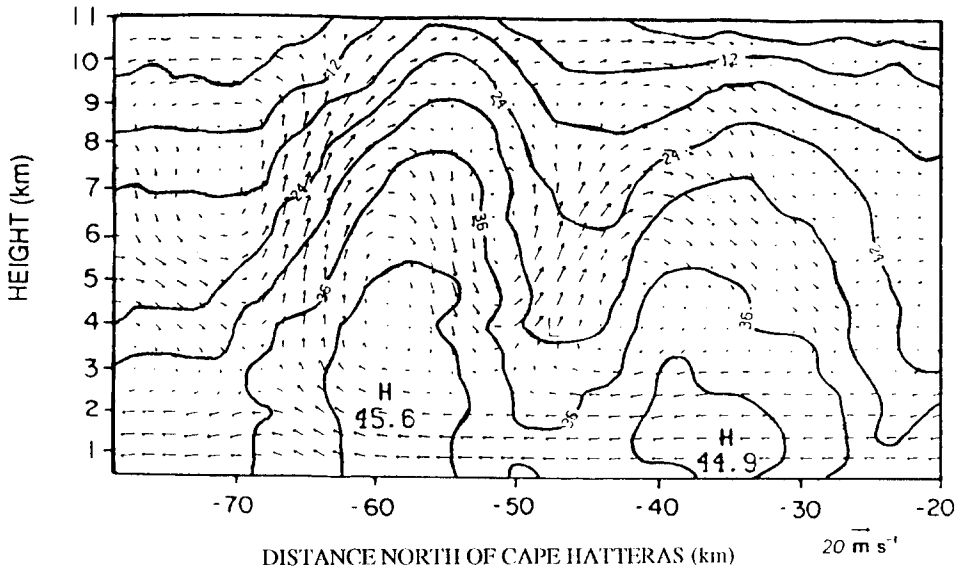

Fig. 6. As for Fig. 4 but for the along-section.

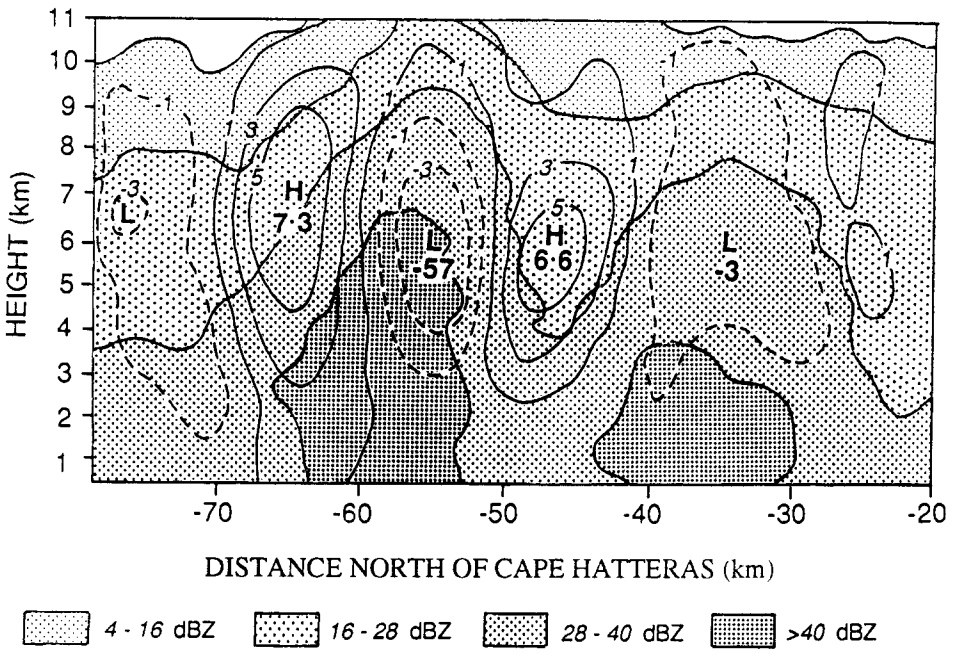

Fig. 7. As for Fig. 5 but for the along-section.

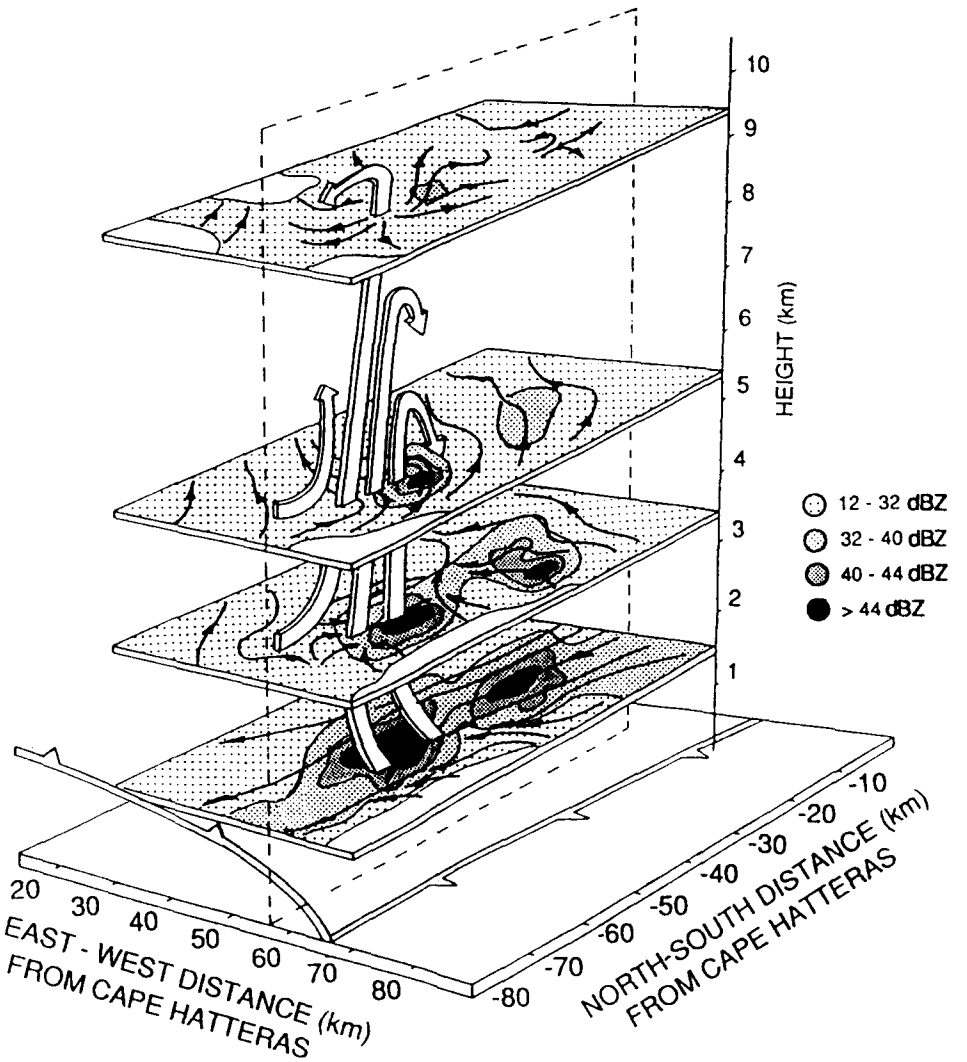

Fig. 8. Three-dimensional depiction of radar reflectivity (units dBZ, shaded) and horizontal storm-relative streamlines (solid lines with arrows) at various levels at 2220 UTC on 26 January 1986. The vertical velocity associated with the southern cell is shown between these levels (large white arrows). All data are based on the CP-3 and CP-4 radars. The approximate position of the cold front is indicated by standard symbols. The flow field and radar reflectivity on the lowest level (1.5 km) are also shown in Fig. 2.

and Houze, 1993). The convective updraft, the stratiform region, and the gap between them, are even more apparent in Fig. 5. A deep front-to-rear flow is present from 2 to 10 km altitude. This flow is almost uniform in strength, with maxima at 3.5 and 9 km. A weak rear-to-front flow extends from the rear (western) boundary to the NCFR in a wedge below 1.5 km. The strength of the updraft and the magnitude of the reflectivity in the NCFR are

also similar to those in a squall line. Within the stratiform region there is a net mesoscale updraft above the freezing level (at ~2.7 km) and a downdraft below it.

Averaging across the two cells in the across-section (Fig. 2) smooths the updrafts. The peak updraft in the southern cell (the stronger of the two) was 13 m s^{-1}. Behind the more stratiform region in the across-section, there was a shallow rearward slanting band (around $x = -10$ km in Fig. 4), and a trailing updraft (at $x = -18$ km in Fig. 5). This band was quite short (Fig. 2) and short-lived; it was one of a series of transient shallow rainbands located between the NCFR and the wide cold-frontal rainband, which was situated ~150 km to the west of the NCFR at 2220 UTC (Locatelli et al., 1994).

The storm-relative airflow through the along-section is shown in Fig. 6. In this frame of reference, the wind was northerly at low levels. At middle levels (~4–7 km) the storm-relative wind was mostly southerly. There were two strong updrafts, both located ~10 km to the south of the cells (Fig. 7). The relation between the airflow and the radar reflectivity is reasonable, except perhaps for the strong middle-level downdraft (around $y = -56$ km) in an area of decreasing reflectivity with height, and, more generally, the offset of the airflow structure by ~5–10 km to the south of the reflectivity pattern. This could be due to the rapid evolution of the cells, in which case the vertical motion field would not have been in equilibrium with the hydrometeor field. The offset is not due to 2-D mass balancing because it is present in the original flow field.

An analysis of the 3-D flow (shown schematically in Fig. 8) shows that the low-level flow bypassed the northern cell and fed the updraft of the southern cell (around $y = -63$ km in Fig. 6), which was the deeper and more vigorous of the two cells (Fig. 7). Mass-balancing in 2-D modified the flow pattern somewhat. For example, at the upper levels of the southern cell the updraft diverged in the meridional as well as in the zonal direction (Fig. 8), so the 2-D meridional divergence was enhanced. This, in turn, enhanced the downdrafts to the south and north of the updraft (around $y = -75$ and $y = -54$ km). Another somewhat misleading feature is the base of the updraft associated with the shallower northern cell (Fig. 6). This cell was fed by low-level prefrontal air that originated to the east of the along-section (to the northeast, in a storm-relative frame of reference, Fig. 8). In 2-D the cell is fed mostly by the downdraft to the north of the main cell. In reality, the convergence below the updraft of the northern cell (at ~3 km) was mostly zonal (Fig. 8). In 2-D, this convergence is translated into the meridional plane at the same level (Fig. 6). Therefore, in 2-D the updraft does not originate in the PBL, whereas, in reality, it probably did so, to the east of the section (Fig. 2).

4. Retrieved cloud and thermodynamic structures

Using the combined TMR technique (Geerts and Hobbs, 1991), we derived the distribution of cloud, precipitation, and thermodynamic forcing that are in quasi-equilibrium with the mass-balanced flow field and specified boundary conditions. At the western boundary of the across-section, the temperature (T_{rear} in Fig. 3a) and relative humidity from the 2220 UTC Hatteras sounding were imposed. The eastern boundary conditions were derived from the composited sounding ahead of the NCFR. This sounding was also used for *both* lateral boundaries in the along-section. The lower boundary conditions for pressure, tem-

perature, and relative humidity for the across-section were based on measurements from the NOAA P-3 aircraft (Fig. 2) and an interpolation to the lateral boundaries.

We will discuss first the retrieved hydrometeor distribution because this can be compared with independent observations, thereby providing a measure of confidence in the retrieved thermodynamic fields. The water variables are based on 2 h of iteration, nested within the iterative TMR scheme. Most of the fields are fairly constant after 2 h, except the specific humidity which oscillates rapidly around a stable average in downdrafts.

Next we will discuss the retrieved thermodynamic fields. Internal consistency of these fields can be checked using the momentum validation technique (Gal-Chen and Hane, 1981). Using this technique, a relative error (E_r), based on the horizontal and the vertical momentum conservation equations, was calculated. For the across-section we found $E_r = 0.33$, and for the along-section $E_r = 0.29$. These values are significantly less than the 0.5 critical value obtained by applying the technique to random input (Gal-Chen and Kropfli, 1984); however, they are also significantly larger than a perfect fit ($E_r = 0$).

4.1. Precipitation

Retrieved rain and snow concentrations in the across-section are shown in Fig. 9, where they can be compared with the rain and snow concentrations estimated from radar data (Appendix A).

The freezing level was at an altitude of 2.9 km ahead of the NCFR, dropping to 2.6 km in the Cape Hatteras sounding. The maximum snow concentration derived from the TMR (Fig. 9b) is located downstream of the maximum reflectivity, and snow is transported into the more stratiform region behind the NCFR where it precipitates out. In the NCFR snow grows primarily by the accretion of cloud water (riming) and, secondarily, by vapor deposition. The snow continues to grow by deposition in the trailing stratiform region, primarily near the NCFR (between $x = 20$ and $x = 40$ km), and also west of Cape Hatteras, which explains the secondary snow maximum in this region that coincides fairly well with the observed secondary reflectivity maximum (between $x = 10$ and 20 km in Fig. 5). This secondary maximum is independent of the NCFR: it is caused by two weak updrafts at middle levels (at $x = 0$ km and $x = -18$ km), rather than by downstream transport of cloud ice generated in the NCFR. Compared to the estimates from the radar reflectivity, the peak and integrated concentrations of snow from the TMR are overestimated by 65% and 92%, respectively. One reason for this discrepancy is that frozen hydrometeors with large terminal fallspeeds, such as graupel or hail, are not included in the retrieval model. There is a fairly widespread area of updrafts > 1 m s^{-1} (Fig. 5) in which snow is suspended. Heavily rimed particles (although no hail) were recorded by the P-3 aircraft as it flew through the NCFR (Fig. 2), and growth by riming is predominant in the NCFR; if included in the retrieval model, these ice particles would have fallen out closer to the main updraft. This explains the displacement between the peak values of radar-derived and retrieved snow concentrations (Fig. 9b), and it suggests that the inclusion of graupel improves the microphysical retrieval in NCFRs, in agreement with the findings of Marecal et al. (1993).

The mixing ratio of rain derived from the TMR is concentrated in two areas in the across-section (Fig. 9a). One, due to the melting of snow, is located below the maximum concentration of snow at the freezing level and extends farther to the west below the stratiform

region. The other is at the base of the main updraft feeding the NCFR. This rain, which has fall speeds larger than the updraft, is mostly formed by accretion and autoconversion of droplets condensed in the updraft below the freezing level. The radar reflectivity also indicates two nearly coincidental areas of maximum rain concentration (Fig. 9a, dashed lines). The more western area (from $x=5$ to $x=32$ km) is associated with a stratiform region that is separated from the deep convection. The dominant peak (around $x=56$ km), which has concentrations well above those retrieved, is linked directly to the updraft in the NCFR. The distributions of the water variables (Fig. 9) and the production terms are similar to those described in Rutledge and Houze (1987), who used an idealized flow field to shed light on cloud microphysical interactions between a convective line and the trailing stratiform region.

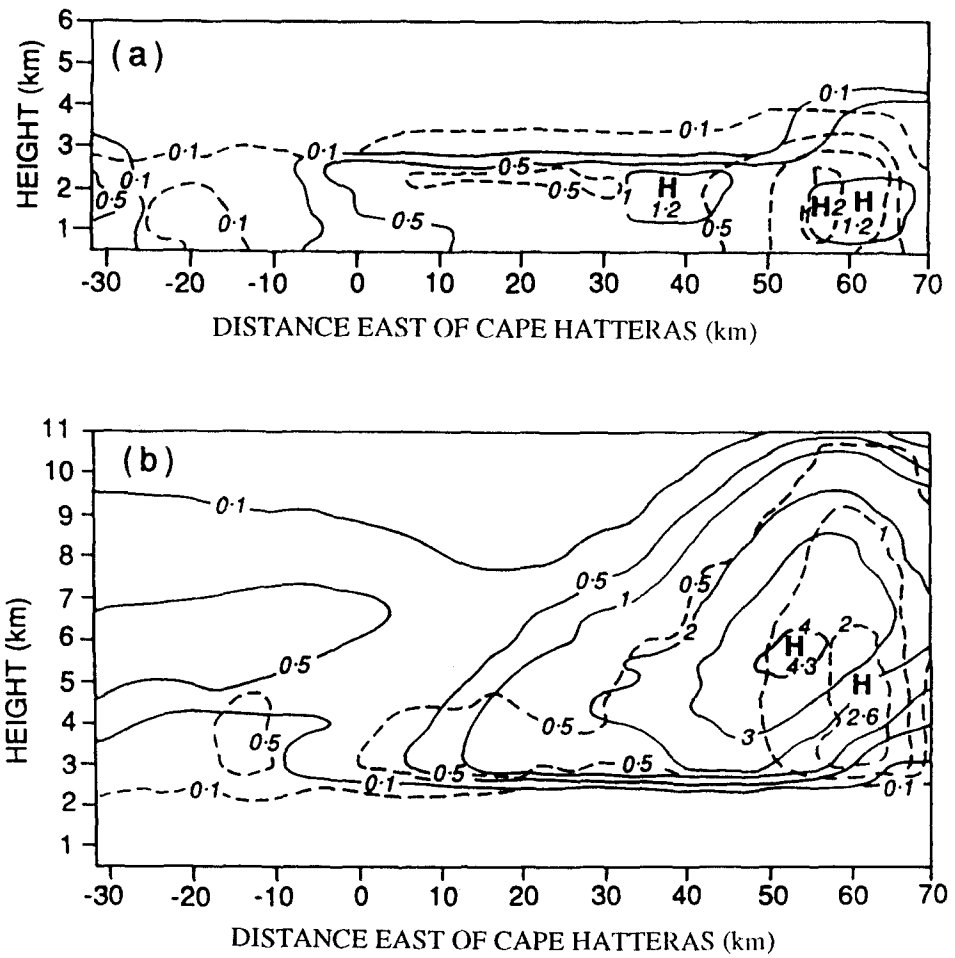

Fig. 9. The retrieved distribution of: (a) rain, and (b) snow (both in g kg^{-1}), for the across-section. The mixing ratios derived from measured radar reflectivities (dashed lines) are also shown.

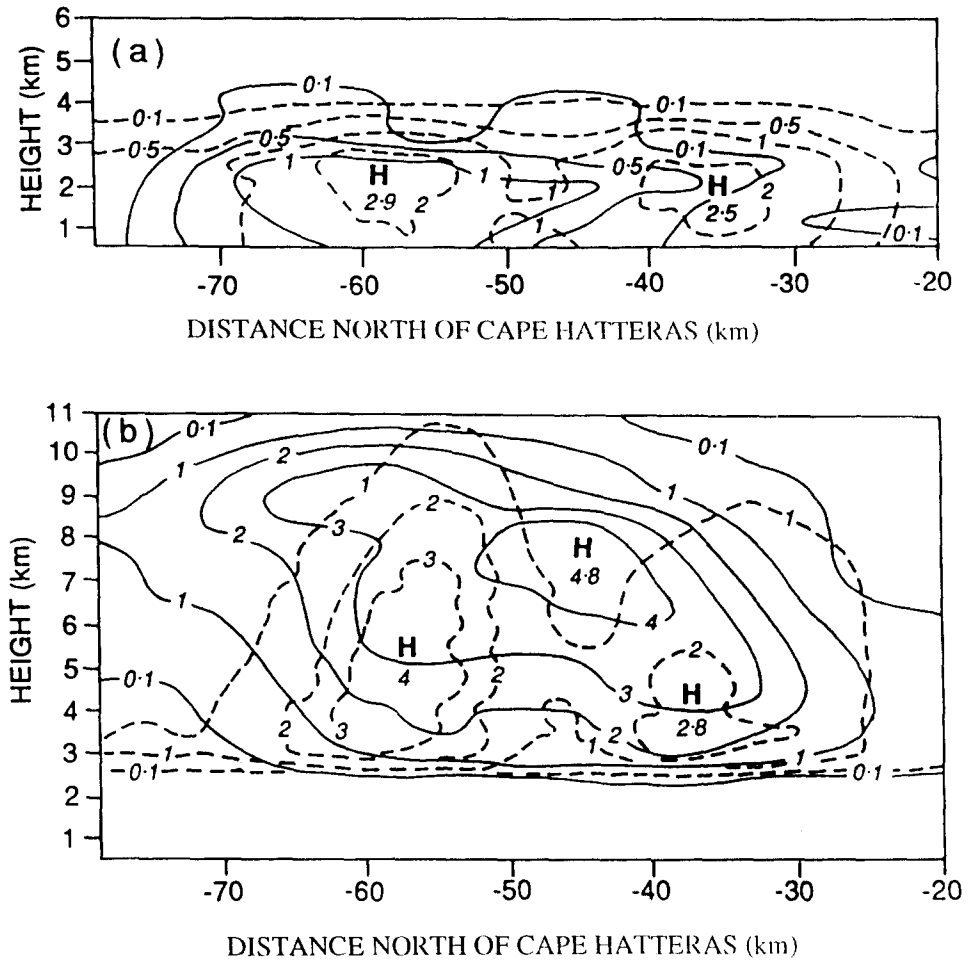

Fig. 10. As for Fig. 9 but for the along-section.

The retrieved distribution of snow in the along-section shows a peak concentration at a higher altitude than suggested by the radar reflectivity (Fig. 10b). Snow decreases with height above the freezing level. Also, the retrieved distribution of snow shows just one broad cell, which is centered roughly between the two cells in the radar reflectivity (Fig. 10b).

The decrease of snow with height is consistent with the flow field: snow evaporates in the two downdrafts and grows (mainly by deposition) in the updrafts (which have a strength larger than the fallspeed of snow). The merging of the two (updraft) cells into one (snow) cell in the TMR is an artifact of the reduction to 2-D. A streamline map of the velocity field (Fig. 6) shows that the southern updraft is directly connected to the northern updraft via the central downdraft, which is not deep enough to evaporate the snow. Therefore, snow is transported from the southern into the northern updraft. In reality, the central downdraft

was southwest of the northern updraft, which was fed by prefrontal PBL air east of the along-section (Fig. 8). Therefore, the two cells were independent.

The TMR shows little rain reaching the ground from the snow generated in the northern updraft (Fig. 10a); this is because of the widespread deep downdraft downstream of the northern updraft. In the retrieval most of the rain falls downstream of the southern updraft, which is based at low levels (Fig. 6). Here rain is produced by the accretion and autoconversion of cloud water, as well as by the melting of snow.

The above discussion suggests that the TMR results for the across-section are more reliable than for the along-section.

4.2. *Thermodynamic structure*

The air buoyancy in the NCFR was retrieved through the optimal combination of two constraints: the vertical momentum conservation equation and the first law (Geerts and Hobbs, 1991). Therefore, buoyancy anomalies (and temperature perturbations) can be produced by latent heating (or cooling), as well as by dynamic requirements (e.g., the maintenance of a strong updraft in the presence of heavy hydrometeor loading). These facts are needed to interpret the retrieved distribution of equivalent potential temperature θ_e (Fig. 11 and Fig. 13).

The θ_e profile on the eastern boundary of the across-section (Fig. 11) was derived from the contrived sounding ahead of the NCFR (dropsonde below and NGM model data aloft). The latent heat released by the freezing of ~ 4.3 g kg^{-1} (the retrieved maximum snow and ice concentration, Fig. 9b) can lift an undiluted air parcel ~ 0.5 km above its level of neutral buoyancy (i.e., up to 10 km altitude in this case). This is still 2–3 km lower than the observed maximum cloud top, and some air can be seen being transported upwards through

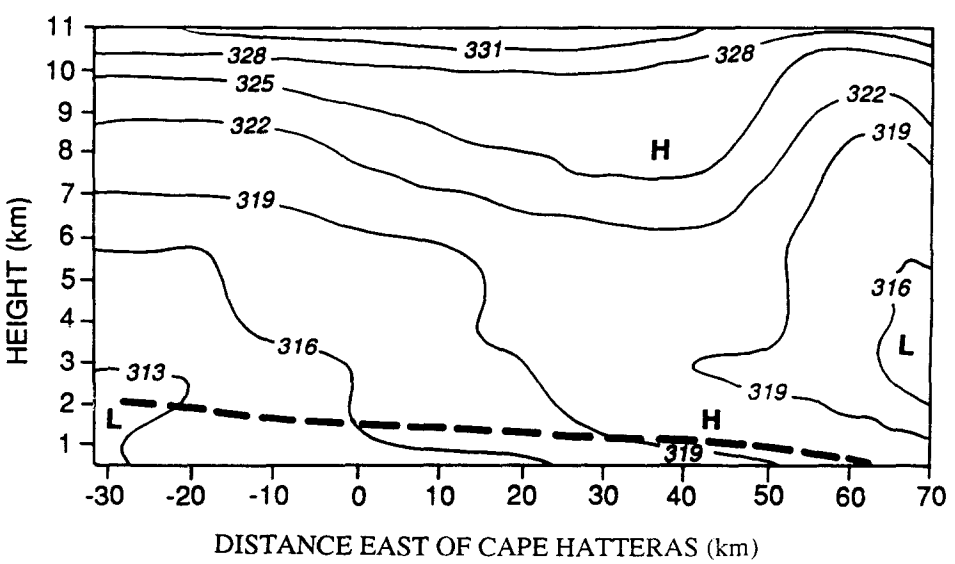

Fig. 11. The retrieved distribution of equivalent potential temperature θ_e (K) in the across-section.

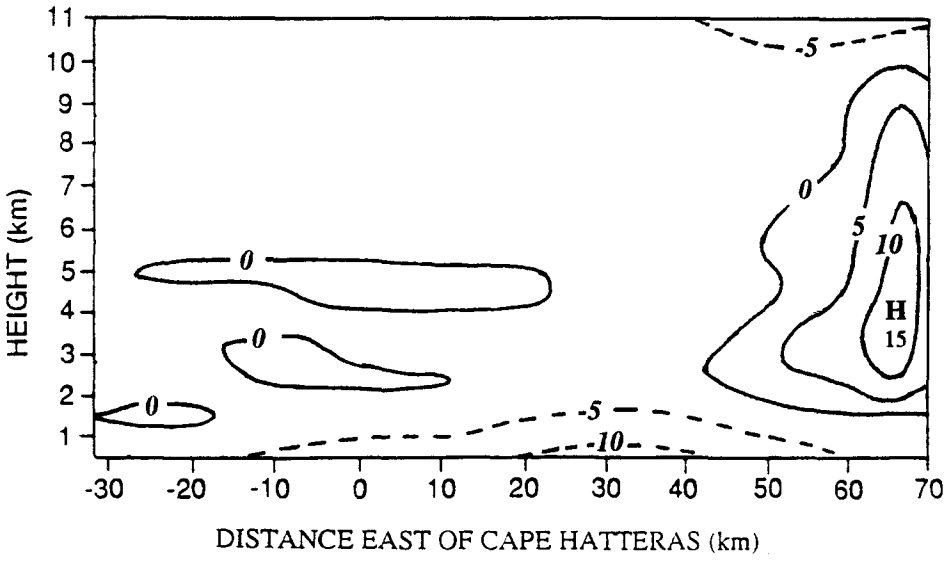

Fig. 12. The retrieved distribution of total buoyancy (in 10^{-2} m s^{-2}) in the across-section. Negative contours are dashed. The reference state is found along the western boundary.

the top of the model domain at 11 km (Fig. 4). The profile based on the NGM model does not show a well-defined tropopause: more stable conditions prevail above 8 km, and there is an isothermal layer above 10.5 km. If the tropopause height in the NGM model is representative of the larger scale environment, then the contraction of the tropopause to a

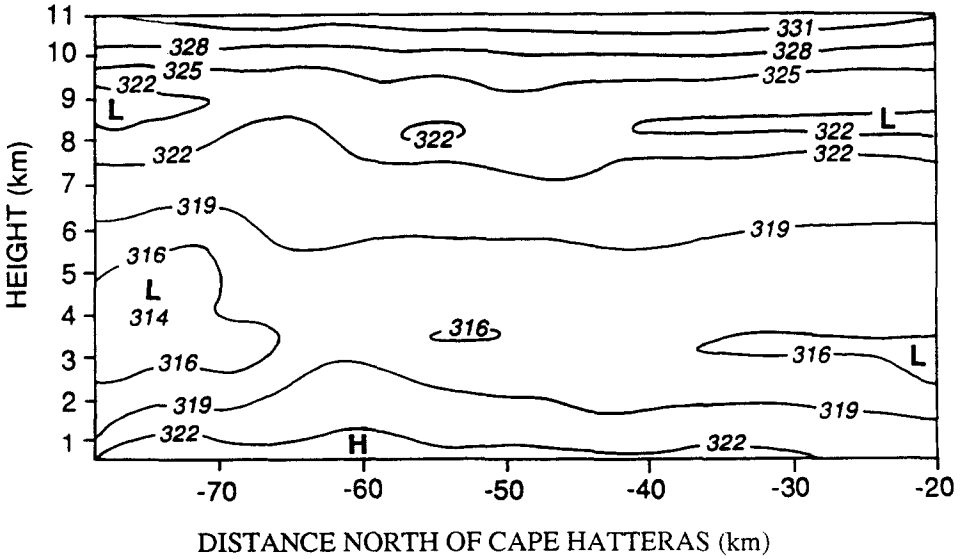

Fig. 13. As for Fig. 11 but for the along-section.

lid at 12–13 km over the NCFR must be due to deep convection "pounding" on the tropopause. This effect is seen in a numerical simulation of a squall line by Fovell et al. (1992). The pounding creates a pool of negative buoyancy at cloud top. Such buoyancy is found at the top of the model domain (11 km) over the NCFR (Fig. 12).

The retrieved peak positive buoyancy with respect to the left border is 0.15 m s^{-2} (Fig. 12). This value is similar to that for a tropical squall line (Roux, 1988), but it is much larger than that of a more typical NCFR (Roux et al., 1993). At the location of peak buoyancy in the NCFR, the temperature perturbation contributes 0.15 m s^{-2}, the water vapour perturbation 0.02 m s^{-2}, and the water loading -0.03 m s^{-2}.

The air was conditionally neutral or stably stratified to the rear of the NCFR, particularly at the lowest levels where cold air had penetrated. The position of the cold-frontal surface is marked by a sudden increase in stability (Fig. 11). This surface corresponds with a sudden wind shift (Fig. 3b and 4). To the rear of the across-section the frontal surface is more horizontal. Within the across-section, the temperature drops by ~ 6.5°C near the surface (Fig. 3 and Fig. 11). This implies strong cold advection, even though the rear-to-front flow in this region is weak. Advective and evaporative cooling can be estimated from the storm-relative airflow and the retrieved temperature and humidity fields. Below 2 km height, west of $x = 50$ km in the across-section, the average cold advection in the zonal direction is 0.58°C h^{-1}, compared to an average net cooling by evaporation of only 0.16°C h^{-1}.

When combined with the wind field, the retrieval results indicate that some areas to the rear of the NCFR above the frontal surface were conditionally symmetrically unstable in the plane normal to the NCFR (not shown). This was due to low stability (Fig. 11) and strong southerly shear at low levels above the front (1.5–3 km, Fig. 3b). The presence of such instability may explain the shallow short-lived rainbands mentioned in Section 2; although it is possible that these rainbands were merely convectively unstable, since the θ_e lines are nearly vertical. The easternmost of these rainbands (Fig. 2) was tilted in a way predicted by symmetric instability (Fig. 4).

The distribution of retrieved θ_e in the along-section is shown in Fig. 13. The lateral inflow boundaries are the same in this section. Not surprisingly the horizontal gradients are small. The atmosphere is potentially unstable in the lowest 3–4 km. Vertical variations in θ_e are somewhat less in the regions with strong vertical motions (from $y = -70$ to $y = -40$ km in Fig. 7). At any one level the minima in θ_e were generally located in downdrafts, where the relative humidity was lower, and the maxima in θ_e were prevalent in updrafts, to some extent conserving θ_e.

4.3. Dynamical structure

Thermodynamic retrieval methods generally suffer from uncertainties in interpreting the vertical gradients (e.g., Lin et al., 1986). The derivation of pressure perturbations in a vertical plane solves this problem (Geerts and Hobbs, 1991). The retrieved pressure in the across-section is shown in Fig. 14 as a perturbation with respect to the left boundary. Because a strong southerly flow exists above the front (Fig. 3b), the ageostrophic part of the perturbation pressure is also shown. This is obtained by removing the zonal pressure variation in balance with the actual meridional wind, starting at the left boundary.

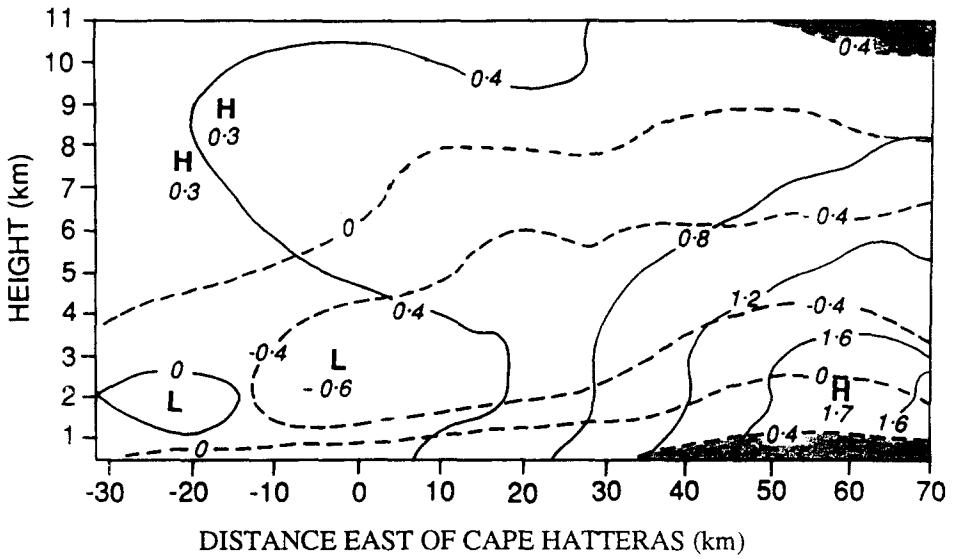

Fig. 14. The retrieved distribution of pressure (in hPa) in the across-section. The pressure is expressed as a perturbation with respect to the western boundary. The total pressure is indicated by the solid lines and the ageostrophic part by the dashed lines. Areas with ageostrophic pressure perturbations exceeding 0.4 hPa are shaded.

In terms of ageostrophic pressure, a high-pressure center is located under the NCFR and there is a meso-low to the rear of the NCFR at low levels. Fig. 14 suggests a low-level low ahead of the NCFR. This pressure distribution is similar to that observed in the vicinity of squall lines (e.g., see fig. 16.5b in Hane, 1986, fig. 16c in Lin et al., 1986, and fig. 9f in Roux, 1988). In these examples of squall lines the geostrophic part of the pressure perturbation is not subtracted, because the cross sections are shorter and the wind parallel to the squall line is weaker.

In analyzing the pressure field it is useful to decompose the geostrophic pressure perturbations into a dynamic and a buoyancy source (e.g., Houze, 1993, pp. 224 and 288). In an isentropic atmosphere on an f-plane, the pressure perturbation field can be diagnosed from the Poisson equation:

$$-\theta_{vb}\nabla^2\pi' = \underbrace{\left\{\left(\frac{\partial u}{\partial x}\right)^2+\left(\frac{\partial v}{\partial y}\right)^2+\left(\frac{\partial w}{\partial z}\right)^2\right\}}_{\text{Ia}} + \underbrace{2\frac{\partial u}{\partial y}\frac{\partial v}{\partial x}}_{\text{Ib}} + \underbrace{2\boldsymbol{S}\cdot\nabla_H w}_{\text{Ic}} + \underbrace{\frac{g}{\rho_b}\frac{\partial \rho'}{\partial z}}_{\text{II}} \quad (1)$$

where (u,v,w) are the velocity components in the (x,y,z) directions, θ_v the virtual potential temperature, π the Exner function, $\boldsymbol{S} \equiv (\partial u/\partial z, \partial v/\partial z)$ the wind shear, and r the air density. The subscript b indicates the basic state, and the prime ($'$) a perturbation. The left-hand term has a distribution similar to the pressure perturbation itself. The first three terms on

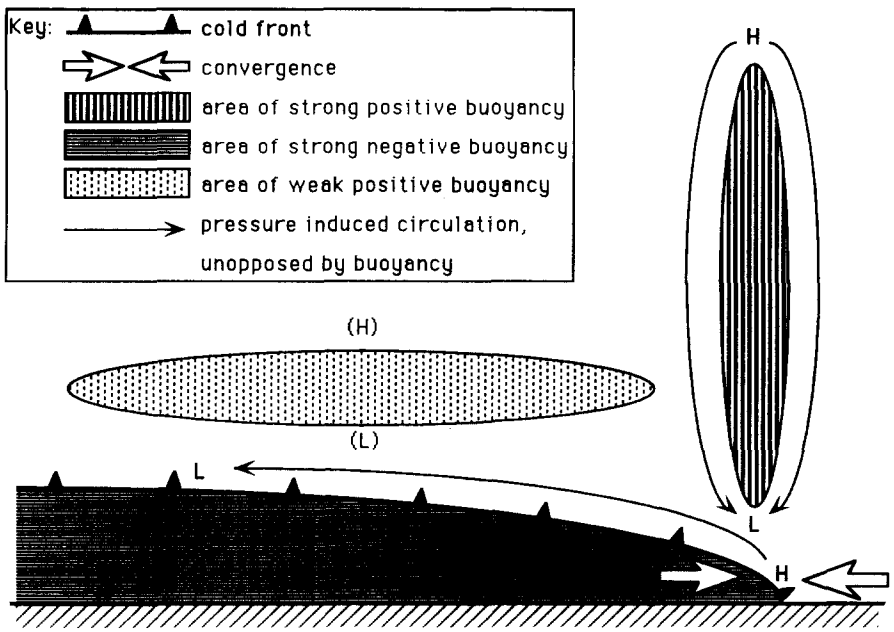

Fig. 15. Schematic representation of the effects of frontal convergence and buoyancy on pressure perturbations in a squall-like NCFR. (*H*) and (*L*) indicate regions of high and low pressure, respectively.

the right of Eq. (1) constitute the dynamic source, consisting of a convergence term (Ia), a vorticity term (Ib), and a shear term (Ic). The fourth term (II) on the right of Eq. (1) is the buoyancy source. A high-pressure anomaly occurs in regions of strong convergence or divergence (Ia). High vorticity (Ib), cyclonic or anticyclonic, is associated with a low-pressure anomaly. The shear term (Ic) predicts a high-pressure anomaly on the upshear side of an updraft. Air buoyancy (II) in convective circulations is opposed by the buoyancy-induced vertical pressure perturbation gradient, which establishes a circulation pattern over an area larger than a buoyant core (e.g., Mapes, 1993). This implies that the buoyancy-induced pressure perturbation field has a minimum value below a buoyant core, and a maximum value above the core. The buoyancy source also explains a high-pressure anomaly under a cold pool (e.g., under a cold-frontal surface); the resulting upward pressure gradient force cancels the negative buoyancy force to produce hydrostatic balance.

In our across-section the shear term is of little importance since the shear in the NCFR is small (Fig. 4). There is more shear in the frontal zone, but there is no strong vertical motion in this region. The dominant dynamic source is the convergence term, which produces a high near the surface (0.7 hPa) and a weaker high (0.4 hPa) near the top of the domain at $x = 60$ km (the position of the NCFR). Isolating the buoyancy source, we find a high under the frontal surface (shown in Fig. 11) and a downward pressure perturbation gradient force in the NCFR, from the top to 3.5 km, where the pressure anomaly is lowest (-0.6 hPa). The effect of buoyancy and convergence on the perturbation pressure field is shown schematically in Fig. 15.

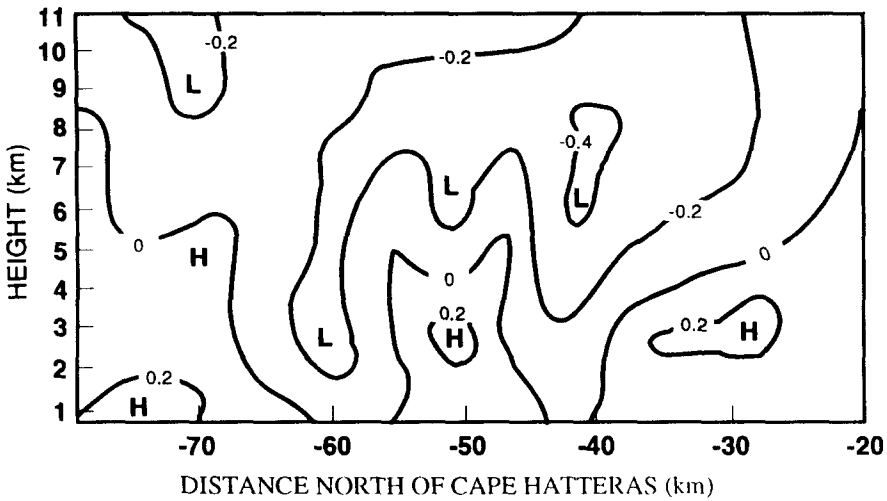

Fig. 16. As for Fig. 14 but for the along-section and relative to the northern boundary.

Clearly, the high-pressure anomaly at low levels near the NCFR (Fig. 14, dashed lines) is primarily due to frontal convergence. Because no Doppler radar data were available below 1 km near the NCFR, the frontal forcing is only partly captured. The upward pressure perturbation gradient from 5 km to the top (Fig. 14) is mainly due to buoyancy forcing (Fig. 12). In the stratiform region the atmosphere is largely hydrostatically balanced, even above the frontal surface. For example, weak positive buoyancy is found in patches between 2.5 and 5.5 km altitude to the rear of the NCFR (Fig. 12). This force is opposed by the perturbation pressure gradient force in the same region (Fig. 14).

The low-level upward pressure perturbation gradient force in the NCFR is only at most 0.03 m s^{-2} (between 1 and 2 km altitude), which is only about one-fifth of the peak buoyancy (Section 4.2). It seems, therefore, that while the convection was triggered by frontal convergence, it was driven primarily by buoyancy. The cellular appearance of the NCFR, and the rapid evolution of the cells that comprised it, attest to its convective nature.

The retrieved pressure perturbations are small in the along-section (Fig. 16) and the geostrophic part is negligible (therefore, the ageostrophic pressure distribution is not shown). While the buoyancy relative to the Cape Hatteras sounding is generally fairly large ($\sim$0.10 m s^{-2}), it is small relative to the (already buoyant) upstream sounding. Because the upstream sounding is used as reference state for the perturbation variables in the along-section, the retrieved buoyancies and buoyancy-induced pressure perturbations are small.

Large horizontal gradients of vertical velocity occur in the along-section (Fig. 7), as well as a large vertical shear of the horizontal wind (Fig. 6). Therefore, in a north–south section through the NCFR the convection is strongly sheared (Fig. 3b), which affects the retrieved pressure perturbations through the shear term [Ic in Eq. (1)] (Rotunno and Klemp, 1982). The pressure (Fig. 16) is shifted horizontally by a quarter of a wavelength upshear (i.e., to the left) with respect to the vertical velocity, as predicted by Eq. (1). In other words,

pressure gradients are centered near, or just below, areas of strong vertical motion. The high anomalies occur beneath upward pressure gradient forces (Fig. 16), which accelerate air upwards. Therefore, this pressure distribution acts to move the cells upshear. We are unable to verify this, because there is no measure of the along-band movement of a NCFR that is independent of the motion of the cells.

5. Conclusions

In this paper we have used the combined TMR technique, based on Doppler radar data, thermodynamic and cloud microphysical boundary values, the equations of motion, and bulk cloud parameterizations, to describe the dynamic and cloud microphysical structures of a line of deep convection along a cold front (i.e., a NCFR).

The principal conclusions of this study can be summarized as follows:

(1) Sounding data, Doppler radar data, and the retrieved thermal structure confirm that the NCFR was triggered and maintained by a surface cold front. The cold front was very shallow (~ 2 km) compared to the NCFR (~ 12 km). The NCFR was identifiable for ~ 6 h and was highly cellular; the cells were shorter-lived (0.5–1 h).

(2) In contrast with several previous studies of NCFRs, the updraft associated with the NCFR described here was driven primarily by buoyancy, due to cold air overlying a well-developed boundary layer over the Gulf Stream. A considerable amount of moist static energy was available, which was released suddenly with the passage of the cold front. This produced large updraft velocities (~ 10 m s^{-1}).

(3) The structure, depth and intensity of the NCFR were similar to a squall line. Trailing behind the NCFR was a region of stratiform precipitation, which had many of the attributes of the stratiform regions trailing behind some squall lines: ice transfer from the NCFR to the trailing region by the front-to-rear flow; a mesoscale updraft in the trailing region above the freezing level (which enhanced ice crystal growth mainly by deposition); and evaporative cooling in the shallow rear-to-front flow. There was, however, one important difference between the NCFR and a squall line: the air behind the stratiform region following the NCFR was significantly cooler in the lowest 2–2.5 km (Fig. 3a). In other words, there was strong cold advection in the rear-to-front flow, and the leading edge of this flow was a cold front. Evaporative cooling, which is responsible for the mesoscale downdraft in the trailing stratiform regions of squall lines and which maintains the cold pool from which the gust front emerges, was of less importance in the NCFR. The dominance of cold advection over evaporative cooling provides a diagnostic distinction between a NCFR and a squall line.

(4) Pressure perturbations near the NCFR confirm its dual nature: they were caused mainly by frontal convergence and buoyancy opposition. The latter established a compensating circulation around the NCFR. Pressure perturbations within the NCFR were due mainly to strong cellular updrafts in the presence of wind shear parallel to the NCFR. In the more stratiform region behind the NCFR the perturbations were close to a hydrostatic balance.

This study suggests that the inclusion of graupel in the bulk cloud scheme improves TMR results for NCFRs. This conclusion is based on our analysis of the air flow, and the cloud and dynamic structures in sections across and along the NCFR. To ensure the representa-

tiveness of these two sections, they were averaged over as wide a domain as possible. Since the retrieved cloud and dynamic structures are based on the 2-D flow, the question remains how 3-D effects would alter the retrieval results.

Acknowledgements

We thank John Locatelli, who designed Fig. 1 and Fig. 8, and Brian Mapes and Mary Barth-Brock for useful discussions. This research was funded by grant ATM-8809061 from the Atmospheric Research Section of the US National Science Foundation, and by grant 20422415 from the Australian Research Council.

Appendix A

Empirical relations between radar reflectivity (dBZ) and the mass mixing ratios of rain (q_r) and snow (q_s) were derived from the maximum reflectivities measured by the CP-3 and CP-4 radars and values of q_r and q_s estimated from simultaneous airborne measurements along a series of flight tracks through the NCFR and its trailing region at various levels, ending with the two tracks shown in Fig. 2. The relations are of the form:

$$q = a\ 10^{-6} \exp(b\ \mathrm{dBZ}) \qquad \text{(A-1)}$$

where q (q_r or q_s) is expressed in kg kg^{-1}. The constants a and b are listed in Table 1.

Precipitation is considered convective in a column if the maximum vertical velocity (up or down) exceeds 1.5 m s^{-1} in the column itself, and in at least one adjacent one. In transition regions, between convective and stratiform precipitation and between snow and rain, a linear combination of Eqs. (A-1a)–(A1-d) is used. The bright band is not explicitly accounted for. Eqs. (A-1a)–(A1-d) compare fairly well to those used in Rutledge and Hobbs (1984) for a NCFR, and to the equation for convective rain suggested by Brown and Braham (1963).

Table A-1
Values of the constants used in Eq. (A-1)

Hydrometeor type	a	b	Eq.
Convective rain	4.4	0.141	(A-1a)
Convective snow	$7.6/\rho_b$	0.148	(A-1b)
Stratiform rain	7.7	0.136	(A-1c)
Stratiform snow	$16.1/\rho_b$	0.139	(A-1d)

References

Biggerstaff, M.I. and Houze, Jr., R.A., 1991. Kinematic and precipitation structure of the 10–11 June 1985 squall line. Mon. Weather Rev., 119: 3035–3065.

Biggerstaff, M.I. and Houze, Jr., R.A., 1993. Kinematics and microphysics of the transition zone of a mid-latitude squall line system. J. Atmos. Sci., 50, 3091–3110.

Bond, N.A. and Fleagle, R.G., 1985. Structure of a cold front over the ocean. Q.J.R. Meteorol. Soc., 111: 739–759.

Brown, E.N. and Braham, Jr., R.R., 1963. Precipitation particle measurements in cumulus congestus. J. Atmos. Sci., 20: 23–28.

Browning, K.A. and Harrold, T.W., 1970. Air motion and precipitation growth at a cold front. Q.J.R. Meteorol. Soc., 96: 369–389.

Carbone, R., 1982. A severe frontal rainband, Part I: Stormwide hydrodynamic structure. J. Atmos. Sci., 39: 258–279.

Chong, M., Amayenc, P., Scialom, G. and Testud, J., 1987. A tropical squall line observed during the COPT81 experiment in West Africa, Part I: Kinematic structure inferred from dual-Doppler data. Mon. Weather Rev., 115: 670–694.

Dirks, R.A., Kuettner, J.P. and Moore, J.A., 1988. Genesis of Atlantic Low Experiment: an overview. Bull. Am. Meteorol. Soc., 69: 148–160.

Fovell, R.G. and Ogura, Y., 1988. Numerical simulation of a midlatitude squall line in two dimensions. J. Atmos. Sci., 45: 3846–3879.

Fovell, R.G., Durran, D.R. and Holton, J.R., 1992. Numerical simulations of convectively generated gravity waves in the atmosphere. J. Atmos. Sci., 49: 1427–1442.

Gal-Chen, T. and Hane, C.E., 1981. Retrieving buoyancy and pressure fluctuations from Doppler radar observations: a status report. NCAR Tech. Rep. No. 13, pp. 98–104.

Gal-Chen, T. and Kropfli, R.A., 1984. Buoyancy an pressure perturbations derived from dual-Doppler radar observations of the PBL: applications for matching models with observations. J. Atmos. Sci., 41: 3007–3020.

Geerts, B. and Hobbs, P.V., 1991. The organization and structure of clouds and precipitation on the Mid-Atlantic Coast of the USA, IV: Retrieval of thermodynamic and cloud microphysical structures of a frontal rainband from Doppler radar data. J. Atmos. Sci., 48: 1287–1305.

Hane, C.E., 1986. Extratropical squall lines and rainbands. In: P.S. Ray (Editor), Mesoscale Meteorology and Forecasting, 1986, Ch. 16. Am. Meteorol. Soc., 793 pp.

Hauser, D. and Amayenc, P., 1986. Retrieval of cloud water and water vapour contents from Doppler radar data in a tropical squall line. J. Atmos. Sci., 43: 823–838.

Hobbs, P.V., 1978. Organization and structure of clouds and precipitation on the mesoscale and microscale structure of cyclonic storms. Rev. Geophys. Space Phys., 16: 741–755.

Hobbs, P.V. and Biswas, K.R., 1979. The cellular structure of narrow cold-frontal rainbands. Q.J.R. Meteorol. Soc., 105: 723–727.

Hobbs, P.V. and Persson, P.O.G., 1982. The mesoscale and microscale structure and organization of clouds and precipitation in midlatitude cyclones, V: The substructure of narrow cold-frontal rainbands. J. Atmos. Sci., 39, 280–295.

Houze, Jr., R.A., 1993. Cloud Dynamics. Academic Press, New York, NY, 573 pp.

Houze, Jr., R.A., Rutledge, S.A., Biggerstaff, M.I. and Smull, B.F., 1989. Interpretation of Doppler weather radar displays of midlatitude mesoscale convective systems. Bull. Am. Meteorol. Soc., 70: 608–619.

Lilly, D.K., 1986. The structure, energetics and propagation of rotating convective storms, Part II: Helicity and storm stabilization. J. Atmos. Sci., 43: 126–140.

Lin, Y.J., Wang, T.C. and Lin, J.H., 1986. Pressure and temperature perturbations within a squall line derived from SESAME dual-Doppler data. J. Atmos. Sci., 43: 2302–2327.

Locatelli, J.D., Martin, J.E. and Hobbs, P.V., 1994. A wide cold-frontal rainband and its relationship to frontal topography. Q.J.R. Meteorol. Soc., 120: 259–275.

Mapes, B.E., 1993. Gregarious tropical convection J. Atmos. Sci., 50: 2026–2037.

Marecal, V., Hauser, D. and Roux, F., 1993. The 12/13 January 1988 narrow cold-frontal rainband observed during MFDP/FRONTS 87, Part I: Microphysics. J. Atmos. Sci., 50: 975–998.

Martin, J.E., Locatelli, J.D. and Hobbs, P.V., 1990. Organization and structure of clouds and precipitation on the Mid-Atlantic coast of the USA, Part III: The evolution of a middle-tropospheric cold front. Mon. Weather Rev., 118: 195–217.

Martin, J.E., Locatelli, J.D. and Hobbs, P.V., 1993. Organization and structure of clouds and precipitation on the Mid-Atlantic coast of the USA, Part VI: The synoptic evolution of a deep tropospheric frontal circulation and attendant cyclogenesis. Mon. Weather Rev., 121: 1299–1316.

Parsons, D.B., 1992. An explanation for intense frontal updrafts and narrow cold-frontal rainbands. J. Atmos. Sci., 49: 1810–1825.

Parsons, D.B., Mohr, C.G. and Gal-Chen, T., 1987. A severe frontal rainband, Part III: Derived thermodynamic structure. J. Atmos. Sci., 44: 1615–1631.

Riordan, A.J., 1990. Examination of the mesoscale features of the GALE coastal front of 24–25 January 1986. Mon. Weather Rev., 118: 258–282.

Rotunno, J. and Klemp, J.B., 1982. The influence of the shear-induced pressure gradient on thunderstorm motion. Mon. Weather Rev., 110: 136–151.

Roux, F., 1988. The West African squall line observed on 23 June 1981 during COPT 81: kinematics and thermodynamics of the convective region. J. Atmos. Sci., 45: 406–426.

Roux, F., Marecal, V. and Hauser, D., 1993. The 12/13 January 1988 narrow cold-frontal rainband observed during MFDP/FRONTS 87, Part I: Kinematics and thermodynamics. J. Atmos. Sci., 50: 951–974.

Rutledge, S.A. and Hobbs, P.V., 1984. The mesoscale and microscale structure and organization of clouds and precipitation in midlatitude cyclones, Part XII: Diagnostic modelling study of precipitation development in narrow cold-frontal rainbands. J. Atmos. Sci., 41: 2949–2972.

Rutledge, S.A. and Houze, Jr., R.A., 1987. A diagnostic modelling study of the trailing stratiform region of a midlatitude convective line. J. Atmos. Sci., 44: 2640–2656.

Smull, B.F. and Houze, Jr., R.A., 1985. A midlatitude squall line with a trailing region of stratiform rain: radar and satellite observations. Mon. Weather Rev., 113: 117–133.